Water-rich conditions during titania atomic layer deposition in the 100 °C-300 °C temperature window produce films with TiIV oxidation state but large H and O content variations

Bingbing Xia, Jean-Jacques Ganem, Ian Vickridge, Emrick Briand, Sébastien Steydli, Rabah Benbalagh, François Rochet

HAL Id: hal-03907172
https://hal.sorbonne-universite.fr/hal-03907172

Submitted on 1 Feb 2023

Water-rich conditions during titania atomic layer deposition in the 100°C-300°C temperature window produce films with Ti[IV] oxidation state but large H and O content variations

Bingbing Xia[1], Jean-Jacques Ganem[1], Ian Vickridge[1], Emrick Briand[1], Sébastien Steydli[1], Rabah Benbalagh[2] and François Rochet[2]

1.Sorbonne Université, CNRS, Institut des NanoSciences de Paris (UMR 7588), SAFIR, 75005 Paris, France

2. Sorbonne Université, CNRS, Laboratoire de Chimie Physique, Matière et Rayonnement (UMR 7614), 75005 Paris, France

Corresponding author. Rochet François: francois.rochet@sorbonne-universite.fr; Jean-Jacques Ganem: Jean-Jacques.Ganem@insp.jussieu.fr; Ian Vickridge : ian.vickridge@insp.jussieu.fr

ABSTRACT:

Titania films prepared by atomic layer deposition attract great attention due to the widespread application of the oxide as a photocatalytic material, or more recently, as a promising charge storage material for lithium or proton batteries. We implement here advanced tools (Ion Beam Analysis and X-ray Photoelectron Spectroscopy, aided by Ellipsometry and X-ray Diffraction) to characterize films grown in the 100°C-300°C temperature window, using

tetrakis(dimethylamino)titanium (TMDAT) as the metal precursor and water vapor as the oxidant. We examine the outcomes of the ALD process as a function of the deposition temperature, applying equal oxidant and precursor half-cycle time lengths, which contrasts with common deposition processes where the water half-cycle is considerably shorter than that of the metal precursor. Under the present ALD scheme, n-type conductive films are obtained where the oxidation state of titanium is overwhelmingly Ti^{IV} at all temperatures, while the hydrogen content (O/Ti ratio) varies considerably, from ~15 at% (~1.8) at 100°C to ~3 at% (~2) at 300°C. The ideality of the ALD process is discussed through the identification of nitrogen-containing molecules detected at the oxide surfaces. By extending the structural and compositional range of ALD titania films, new opportunities of application are expected to appear.

1. INTRODUCTION

TiO$_2$ is a multifunctional material, best known for its photocatalytic and photoelectrochemical properties (water splitting),[1][2][3][4][5] but with other emerging applications, most particularly as a charge storage material in Li$^+$ or H$^+$ batteries.[6][7][8][9][10][11] TiO$_2$ is used under a great variety of forms: nanoparticles, mesoporous structures, or compact films according to the sought application. The question we are interested in here is the deposition of thin TiO$_2$ layers via the so-called Atomic Layer Deposition (ALD) technique.[2][4][5][7] A great deal or organometallic precursors and oxidative species can be used (a review is given in ref[12]), but we shall focus here on the combination of an alkylamido organometallic ALD precursor, tetrakis(dimethylamido)titanium (TDMAT, see Figure 1) with water. The Ti-N bond is sufficiently weak to allow deposition at low temperature (100°C and below), and physisorbed water is believed to contribute to the growth rate.[12] On the other hand, at 200°C, a nonideal ALD growth is observed,[13] with imperfect self-saturation behavior of the growth per cycle (GPC) with increasing TDMAT exposure time. Because of the low Ti-N bond strength, an early self-decomposition [14][15][16] of the molecule is proposed as an explanation (see below).[12][13]

Ideally, during ALD deposition, cycles of exposure to TDMAT and H$_2$O are alternated (Figure 1(a)) and TiO$_2$ grows layer by layer via ligand exchange reactions R1 and R2 (the superscript (*) indicates a surface species, and Me is a methyl).

In the TMDAT half-cycle one has:

$$Ti(NMe_2)_4 + TiO_2-OH^* \rightarrow NHMe_2 + TiO_2-O-Ti(NMe_2)_3^* \qquad\qquad R1$$
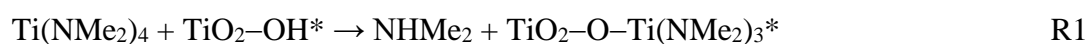
while in the subsequent water half-cycle one has:

$$TiO_2-O-Ti(NMe_2)_3^* + 2H_2O \rightarrow TiO_2-TiO_2-OH^* + 3NHMe_2 \qquad\qquad R2$$

At each step, dimethylamine (NHMe$_2$, DMA) is released to the gas phase.

In this respect, the real-time near ambient pressure X-ray photoelectron spectroscopy (NAP-XPS) study by Head et al.,[17] can be considered as a true test of the ALD process ideality, as TMDAT decomposition in the gas phase is very limited (in the NAP-XPS setup a weak DMA contribution was seen[18]). The ligand substitution mechanism is indeed observed at 110°C in the real-time time NAP-XPS experiment as the component relative to the amido ligand (NMe_2^-) in the N 1s spectra is fully eliminated after each water half-cycle.
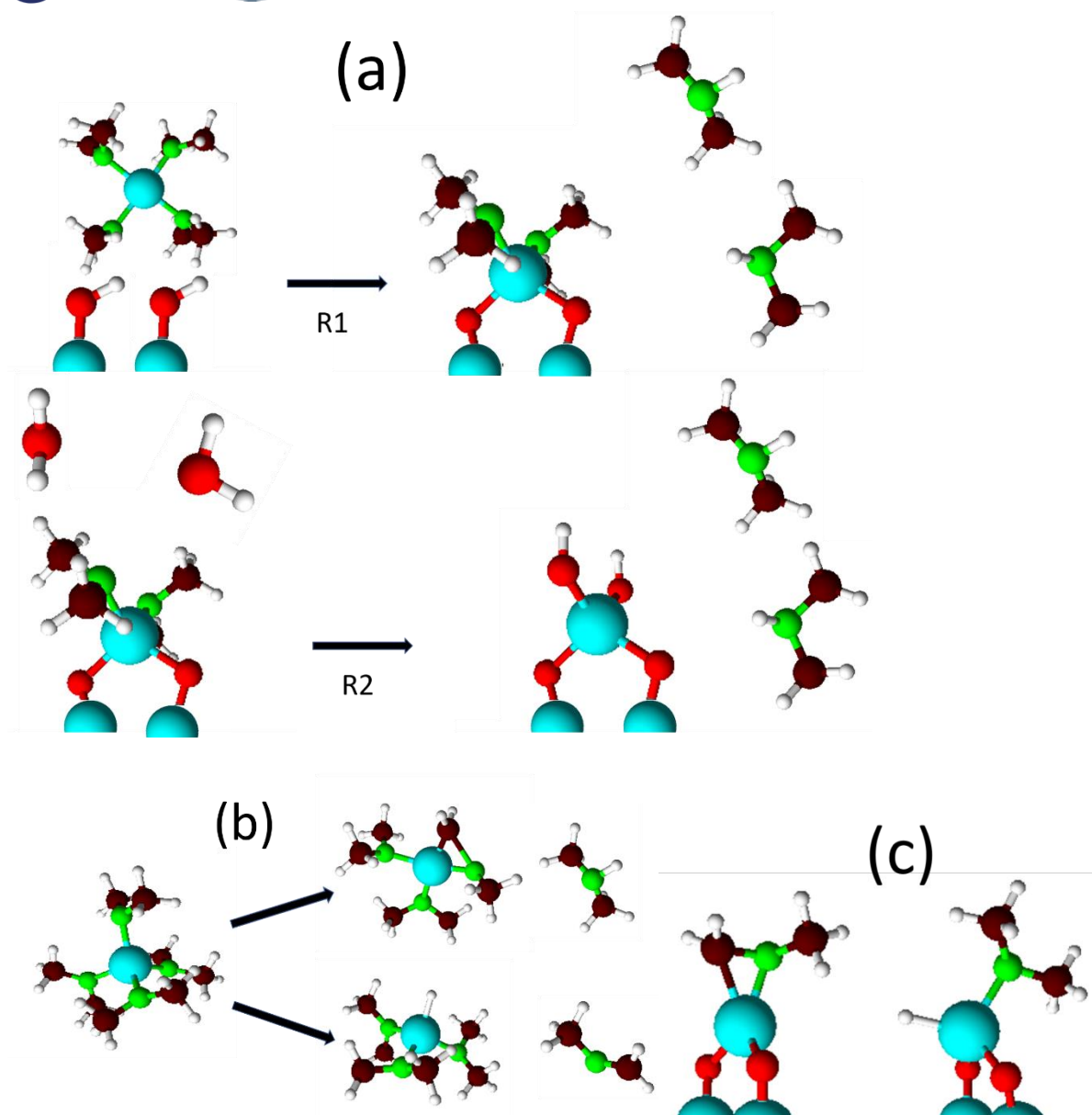
Figure 1. Panel (a): Ligand substitution reactions R1 and R2. For the sake of simplification one Ti atom bonds with four O atoms and one O atom with two Ti atoms (4:2 coordination), while in crystalline phase TiO_2 the coordination is 6:3. Panel (b): the gas phase decomposition products due to β-hydride elimination, the Ti-C-N metallacycle *plus* DMA (top) and $HTi(NMe_2)_3$ *plus* Me-N=CH$_2$ (bottom). Panel (c): two possible surface species resulting from a β-hydride elimination, the Ti-C-N metallacycle (left),[17] and Ti-H (right). Color code: cyan (Ti), maroon (C), red (O), lime (N), white (H).

However, the ligand exchange reactions R1 and R2 (Figure 1(a)), with DMA going into the gas phase, may be an oversimplification of the chemical reactions occurring during the ALD process. First, it should be noted that TMDAT decomposes in the *gas phase* over 140°C.[14] Calculations[16] show that the path with the lower energy barrier (39.0 kcal/mol) corresponds to the transfer of a proton (via the β-hydride elimination) from one amido ligand to a neighboring one to produce the Ti-C-N metallacycle and a DMA dimethylamine molecule (Figure 1(b)). The reaction having the next higher barrier (52.7 kcal/mol) proceeds also via a β-H elimination (also shown in Figure 1(b)) and it produces $HTi(NMe_2)_3$ and the imine Me-N=CH$_2$ (N-methylmethyleneimine). Mass spectrometry supports the formation of the Ti-C-N metallacycle and $HTi(NMe_2)_3$ as the dominant pathways.[15] In thermalized ALD chambers, these gas phase reactions can naturally occur. β-hydride elimination can also occur after the adsorption of TMDAT. In fact, surface reactions competing with the ligand exchange reaction are envisaged, following schemes adopted for gas phase reactions.[17][19] Possible products are depicted in Figure 1(c). The NAP-XPS study of Head et al.[17] points to a Ti-C-N metallacycle (Figure 1(c), left) present on the surface. This species appears from the first TMDAT half-cycle at 110°C and survives the following H$_2$O half-cycles. However, such a species is not always observed.[19] The formation of the Ti-H compound (Figure 1(c), right) can lead to H incorporation and O under-stoichiometry.

A strong motivation of the present study is to demonstrate the added value of coupling ion beam analysis (IBA) with X-ray photoelectron spectroscopy (XPS) to characterize TiO$_2$ films produced by ALD. This synergy was already demonstrated in the case of HfO$_2$ ALD growth [20]. IBA techniques − Rutherford backscattering (RBS), Nuclear reaction analysis (NRA) and elastic recoil detection analysis (ERDA) − present the great advantage of giving an absolute quantification of the atomic species present in the films (expressed in areal densities),

which is of utmost importance considering that residues of a non-ideal ALD process can govern their optical, and electronic properties, as well as their crystallinity.[12] IBA techniques are not limited by surface sensitivity like soft X-ray photoemission spectroscopy (XPS) is. RBS and NRA measurements give access to bulk stoichiometries. Importantly, ERDA can detect H atoms to which XPS is blind, and was proven very useful for the characterization of ALD oxides [21]. Given the potential impact of H interstitials on the reduction of the titanium ion from Ti^{4+} to Ti^{3+},[22][23] knowing the H content is indeed a crucial information. For its part, XPS of core-levels and valence bands is an invaluable technique to unravel the electronic structure and nature of the chemical bonding of the ALD TiO_2 thin films, which is of course inaccessible to IBA techniques. The Ti 2p core-level is particularly sensitive to the oxidation state of titanium,[4][5][17][24] and thus information on the reduction of the oxide can be precisely known down to ~1 atom%. Ti^{3+} ($3d^1$) states can also be detected in the valence band gap.[25][5][4] and their origin (O vacancies[26] or insertion of impurity atoms[22][23]) can be discussed according to their binding energies (BE). Finally, the N 1s spectra provide also information on the chemistry of nitrogen imbedded in the films or present at the surface. As ammonium, amine, amido and Ti-C-N metallacycle species have distinct BEs,[17][5] the identification of adsorbed species provides insight into the surface reactions. Besides the Ti-C-N metallacycle, the NAP-XPS study by Head et al.[17] pointed to the presence of adsorbed DMA and protonated DMA (dimethylammonium or $DMAH^+$). DMA is naturally the product of the ligand exchange reactions R1 and R2, and of the metallacycle reaction.

A second motivation of the study is to relate the ALD half-cycles time programs and growth temperature with the outcomes of the process (stoichiometry, impurity content and its chemistry, oxidation state of the titanium ion, crystallography), taking the specific case of the TMDAT/water couple. So far, most efforts have been devoted to photocatalytic applications with a focus on reduced amorphous TiO_2 films, using low growth temperature and water pulse

durations an order of magnitude shorter than those of TMDAT.[4],[5] Our goal was to explore ALD conditions leading to titanium in its higher oxidation state, adopting a water-to-TMDAT exposure length ratio of about 1, having in mind that the range of application of ALD grown TiO_2 films in the field of energy materials goes beyond photocatalytic materials, as it now involves charge storage materials, such as the new promising TiO_2/ZnO nanolaminar batteries.[7],[10]

2. EXPERIMENTAL SECTION

2.1. Atomic Layer Deposition (ALD)

The TiO_2 thin films were grown by atomic layer deposition (ANRIC AT410 deposition system) on Si(100) (with ~1.8 nm native oxide), using TDMAT and water precursors. The silicon surface cleaned by ultrasonic bath in ethanol (30 min) and acetone (30 min). The metallic precursor and water vapor were transported into the reaction chamber with 50 sccm N_2 carrier gas controlled by a mass flow controller. A long N_2 purge time of 15 s was used to prevent precursor mixing and CVD-like deposition. The precursor bottle and carrier gas line were heated to 62°C to prevent precursor condensation before entering the reaction chamber. The oxide growth was carried out in a (hot wall) reaction chamber thermalized at 100°C, 225°C, and 300°C. A TDMAT pulse time of 1.5 s, and a water pulse time of 2 s were used, always finishing with an H_2O exposure to remove the surface organic groups, followed by the purge in N_2. The pressure of TDMAT is about 6 mTorr during the 1.5s pulse, while the pressure of water is about 3000 mTorr during the 2s pulse.

2.2 Ellipsometry

To monitor the thickness of the TiO_2 thin film, we used Film Sense FS-1[TM] Banded Wavelength Ellipsometer at an incidence angle of 65° and FS-1[TM] software for thickness calculation. The Cauchy model was used to determine refractive index with no surface or

interface roughness.[27] The FS-1^{TM} Ellipsometer records the data at four discrete wavelengths in the visible spectrum: 465nm (blue), 525nm (green), 580nm (yellow), and 635nm (red).

2.3 Grazing Incidence X-ray diffraction (GIXRD)

The phase structure of the ALD TiO_2 samples was determined via grazing incidence X-ray diffraction (GIXRD) using a SMARTLAB bench (diffraction meter 5 circles) with Cu K_α radiation (λ = 1.5406 Å, hν = 8.05 keV) and 45 kV and 200 mA cathode voltage and current, respectively. The samples were scanned in 2θ between 15° and 90° using a grazing-incidence angle of 0.5°.

2.4 Ion beam analysis (IBA)

Ion Beam Analysis (IBA) was carried out at the SAFIR platform at the Institut des Nanosciences de Paris, Sorbonne University (Paris). Ti areal density [Ti] was determined by Rutherford Backscattering Spectrometry (RBS), using a 100 nA 2.0 MeV $^4He^+$ beam of 1mm diameter. The scattered particles were detected at 165° from the beam axis. A reference sample of Bi implanted into silicon, with [Bi] = 5.66 x 10^{15} cm^{-2} (1σ=±2%), was used to calibrate the detector solid angle.[28]·[29]

Nuclear Reaction Analysis (NRA) was used to determine the ^{16}O areal densities [^{16}O] via the $^{16}O(d,p_1)^{17}O$ nuclear reaction. O areal densities were obtained with respect to a ^{16}O standard consisting in a thermal SiO_2 film having an areal density [^{16}O] of 700×10^{15} cm^{-2} (1σ = 2%). An 860 keV deuteron beam was used, with a current of 85 nA in a 2 mm diameter beam spot. The protons produced by the nuclear reactions were detected at 150° from the beam axis in a 300 mm^2 detector covered by a 13 μm mylar foil (used to avoid the saturation of the detector by the high flux of elastically scattered deuterons).[30] The contribution of the native oxide grown on the Si(001) substrate prior to ALD processing ([^{16}O]=7.8×10^{15} cm^{-2}) was systematically subtracted from the [^{16}O] values given in this paper. The nitrogen areal density [^{14}N] was

determined by NRA via the $^{14}N(d,\alpha_1)^{12}C$ nuclear reactions with a 1450 keV deuteron beam of 100 nA in a 2 mm beam spot.[31] An Si_3N_4 sample with $[^{14}N] = 457 \times 10^{15}$ cm^{-2} was used as a reference.

The hydrogen areal density ($[^1H]$) was determined by Elastic Recoil Detection Analysis (ERDA) with an 80 nA 2.0 MeV $^4He^+$ beam incident at a grazing angle of 80°, and recoil detection at 30° scattering angle in a collimated detector behind a 9.15 μm mylar film. An implanted SiH sample with $[H] = 140 \times 10^{15}$ cm^{-2} was used as a reference. The hydrogen depth profile in the TiO_2 films is simulated by the SIMNRA [32]. The (non-Rutherford) recoil cross-section of ref[33] for $H(^4He, H)^4He$ was used.

2.5 Monochromatized X-ray Photoelectron Spectroscopy (XPS)

The XPS setup is installed at "Laboratoire de Chimie Physique, Matière et Rayonnement" (UMR CNRS 7614), and is part of the XPS platform of the "Institut Parisien de Chimie Physique et Théorique" (FR CNRS 2622) of Sorbonne University. The Al K_α monochromatized source (SPECS FOCUS 500, hν=1486.71 eV) was operated at 10 kV, with an anode current of 25 mA (250 W). The electron analyzer was a SPECS PHOIBOS 150, fitted with a delay line detector. The pass energy was 20 V and the entrance slit width was 3 mm. Measurements (Medium Area Mode) were made at normal electron takeoff. The midpoint of the Fermi edge of an Ar-bombarded, clean nickel foil was used to determine the zero of the BE scale. The full width at half maximum (FWHM) of the derivative of the Fermi edge was 360 meV. Therefore, the overall instrumental resolution (photon band width and analyzer resolution) is better than this value considering that the edge is the convolution of the instrumental Gaussian function with the Fermi-Dirac function (k_BT=25 meV at 300 K). For all the samples studied, we used an electron flood gun to compensate possible charge effects. We saw no variations in the BE positions, which indicates that the ~11 nm thick films were sufficiently conductive.

The core-levels were fitted with sums of pseudo-Voigt or Gaussian functions. Stoichiometries and atomic surface concentrations were estimated considering calculated atomic photoionization cross-sections (σ)[34] (measurements are made in the so-called magic angle (54.7°) configuration, to eliminate the contribution of the asymmetry parameter β) and calculated inelastic mean free paths (λ).[35] σ and λ values are reported in Table 1.

Electron Level	$\sigma(h\nu)$ (Mbarn)	BE (eV)	KE (eV)	λ(KE) (Å)
O 1s	0.04005	530.7	956.0	20.8
Ti 2p	0.1069	459.2	1027.5	22.00
N 1s	0.02451	400.6	1086.1	23.0
C 1s	0.01367	285.3	1201.4	24.8
O 2p	2.602×10^{-4}	3	~1480	29.3
Ti 3d	1.894×10^{-4}	7		

Table 1. Values of the cross-sections ($\sigma(h\nu)$), binding energies (BE), kinetic energies (KE) and inelastic mean free paths (λ(KE)) for the core- and valence levels of the elements present in the deposited TiO_2 films. Measurements are made at $h\nu=1486.71$ eV.

The "as-grown" thin films were introduced into the UHV analysis chamber after exposure to air. No further treatment (other than pumping to UHV at room temperature) was made before the XPS measurements. However, after each XPS run (overview, Ti 2p, valence band, C 1s, O 1s, and N 1s recordings), the contamination of the first surface layers of the samples was almost entirely removed by Argon sputter cleaning (1 keV, 10^{-5} mbar, 8 min). Typically, after Ar-bombardment the C 1s to Ti 2p intensity ratio decreases by about an order of magnitude (see supplementary material, section S1, Table S1).

3. RESULTS AND DISCUSSION

ALD cycles ranging from 90 to 160 were applied to obtain the targeted thickness (ca 11 nm), that was measured by ellipsometry. The film preparation conditions, thicknesses and growth per cycle (GPC) are reported in Table 2. The GPC is minimum at 225°C, corresponding to that is called by many authors [36],[37],[38],[39],[40] the "ALD window", while the existence of such a window for TiO_2 deposition from TDMAT is not confirmed in [13][41]. At 100°C the GPC is about 1.4 times greater than that at 225°C. This is generally interpreted as being due to a higher concentration of surface reactive OHs, which leads to a greater availability of reactive centers, and hence to the higher growth rate.[42] The GPC at 300°C is about 1.7 times greater than that at 225°C. In this case, the higher GPC may be indicative of precursor decomposition and adsorption, which leads to a partially CVD-like growth. Consequently, one can expect that the stoichiometry, impurity content and crystallographic structure vary with the growth temperature.

The GIXRD scans given in Figure 2 show that the temperature has a clear impact on the film crystallinity. The "100°C" film is amorphous (no diffraction peaks are observed). On the other hand, diffraction peaks of anatase and of an anatase/rutile mixture are seen for films grown at 225°C and 300°C, respectively. This temperature dependence is in line with the ALD growth of TiO_2 using the reaction between $TiCl_4$ and H_2O. Aarik and coworkers[36] observed by electron diffraction that TiO_2 films are amorphous when grown at temperatures below 165°C, under the anatase form in the 165−350°C range, while rutile dominated at temperatures above 350°C. As advanced by Aarik et al., the explanation for the amorphous structure formed at low temperatures may be that precursor residues hinder the crystallization. However, the reason for the transition to rutile structure at such low temperatures, 300°C here and 350°C in ref [36], remains to be better understood, as in pure synthetic titanium dioxide, the anatase to rutile phase

transition occurs at much higher temperatures, in the 600 °C - 700 °C range.[43] A low temperature transition to rutile has been recently attributed to a low amount of N contamination [44]. The IBA results will indeed show the absence of nitrogen in the oxide bulk (see below).
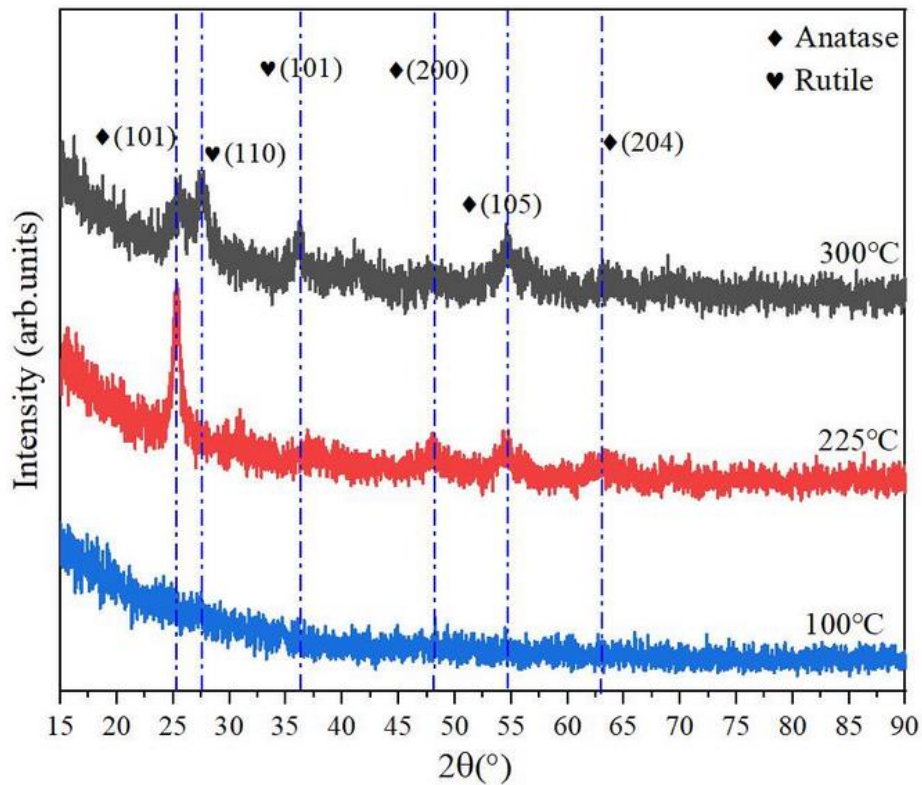
Figure 2. GIXRD study of films formed at 100°C (amorphous), 225°C (anatase diffraction peaks) and 300°C (anatase and rutile diffraction peaks). The peak at 31° (225°C sample) is due to noise.

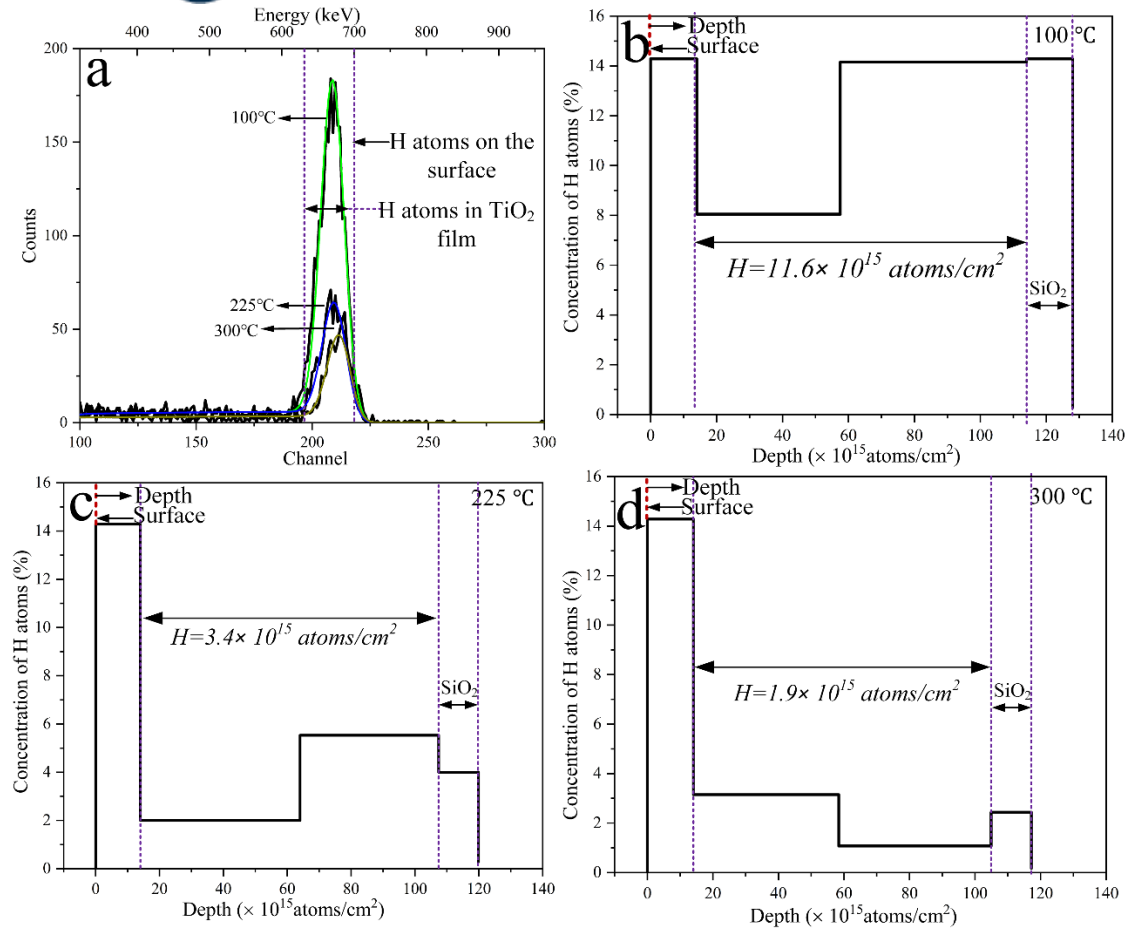Figure 3. ERDA analysis of TiO₂ films grown at different temperatures: (a) ERDA spectra. H atoms depth distribution in the film deposited at (b) 100 °C, (c) 225 °C (ALD window), and (d) 300 °C.

Growth temperature	100°C	225°C	300°C
Water pulse duration (ms)	2000	2000	2000
Number of cycles	120	160	90
h (nm	11.3±0.5	11.1±0.5	11.0±0.5
GPC (nm)	0.094	0.069	0.122
[Ti] 10^{15} cm^{-2}	24.6±0.5	26.5±0.5	27.6±0.5
[^{16}O] 10^{15} cm^{-2}	44.2±1.0	53.9±1.1	55.6±1.2
[^{16}O]/[Ti] 10^{15} cm^{-2}	1.80±0.08	2.04±0.08	2.02±0.08
[^{1}H] 10^{15} cm^{-2}	11.6±0.3	3.4±0.2	1.9±0.2
Density (g.cm^{-3})	2.99±0.06	3.64±0.07	3.85±0.08

Table 2. Ellipsometric thickness *h*, GPC values and IBA atomic areal densities. [Ti], [^{16}O], and [^{1}H] are the areal densities (expressed in 10^{15} cm^{-2}) of the Ti, ^{16}O (the $7.8×10^{15}$ atoms.cm^{-2} of the SiO$_2$ layer are subtracted), and ^{1}H atoms, respectively. The areal density of the ^{14}N atoms is beyond the detection limit of 0.3% in mass. The film density calculated from equation (2) is also given considering the ellipsometric thickness *h*. the water and TDMAT pulse durations are 4×500 ms and 3×500 ms, respectively. Bulk densities of anatase and rutile are 3.78 and 4.23 respectively.

Let us first consider the residues of the precursor (N, C and H) that could be incorporated in the films. A first surprising result is the absence of detectable nitrogen using the $^{14}N(d,\alpha_1)^{12}C$ nuclear reaction, for all of the films. This question will be further addressed in the XPS section (section 3.3). The areal densities of the other elements, [Ti] (obtained by RBS), [^{16}O] (obtained by NRA), and [^1H] (obtained by ERDA) are reported in Table 2. Carbon is observed in the NRA spectra ($^{12}C(d,p_0)^{13}C$ reaction with 860 keV deuterons), but is not reported here. Indeed, XPS shows that the surface, after exposure to air, is contaminated by organic species (see supplementarymaterial, section S1), in particular carboxylic acids. In addition, during the NRA measurement, carbonaceous species resulting from the cracking of residual molecules under the deuteron beam (the pressure is 10^{-5} mbar in the IBA chamber) accumulate at the surface during the IBA measurement. Because of these ambiguities we can confirm neither the presence nor the absence of carbon in the bulk. An upper limit of 1.6 at% for the carbon concentration is derived from the XPS experiments in the supplementary material (section S1) for the Ar-sputtered "225°C" film, assuming that the remaining C is evenly distributed in the depth of the film. However, there are no signs of the presence of C-induced gap states [45] in the valence band spectra in the 225 °C and 300 °C samples.

The ERDA spectra are shown in Figure 3(a) and the corresponding H depth profiles are reported in Figure 3 (b), (c) and (d), for the films grown at 100°C, 225°C and 300°C, respectively. Bulk film hydrogen concentrations were determined from the ERDA spectra after considering the ubiquitous surface contamination and the hydrogen present at the TiO_2/SiO_2 interface and in the native SiO_2 (see Figure 3). The overall hydrogen content (Table 2) in the three films can be compared to each other as their thicknesses are practically equal. [^1H] decreases from ~11.6×10^{15} cm^{-2} to 3.4×10^{15} cm^{-2} as the temperature increases from 100°C to 225°C, and further falls to 1.9×10^{15} cm^{-2} at 300°C. Therefore, at all three temperatures H is present in the bulk of the film. Considering that the surface contamination layer contributes to

$\sim 2 \times 10^{15}$ H cm^{-2}, then the "depth averaged" [^{1}H]/[Ti] ratio is ~ 0.5, ~0.12 and ~0.07 for the films grown at 100°C, 225°C, and 300°C, respectively. For the "100°C" film, the H content corresponds to 0.6 wt%. To give an idea, the H uptake in black hydrogenated titania (H-TiO$_2$) is 0.3 wt%.[46] Such high quantities could impact the electronic structure (as observed in H-TiO$_2$): this point will be discussed below, when XPS data are analyzed.

Besides the H content, another remarkable contribution of IBA is the determination of the atomic ratio [^{16}O]/[Ti] in the thin films, see Table 2. This value is 1.80±0.080 for the 100°C sample, clearly below the stoichiometric value of 2. This indicates that the amorphous oxide is oxygen deficient. In contrast, for the crystalline films grown at 225°C and 300°C samples, a value of 2 enters into the interval of uncertainty of the measured [^{16}O]/[Ti] ratio.

Table 3 also gives the film density ρ as a function of the deposition temperature. To calculate ρ we use the physical thickness h given by ellipsometry and the areal densities [Ti], [^{16}O], and [^{1}H] given by IBA techniques. The molar mass $M_{\mathrm{TiO}_x\mathrm{H}_y}$ is given by:

$$M_{\mathrm{TiO}_x\mathrm{H}_y} = \mathrm{M_{Ti}} + \mathrm{M_O}\frac{[^{16}\mathrm{O}]}{[\mathrm{Ti}]} + \mathrm{M_H}\frac{[^1\mathrm{H}]}{[\mathrm{Ti}]} \tag{1}$$

and ρ is given by:

$$\rho = [\mathrm{Ti}]\frac{M_{\mathrm{TiO}_x\mathrm{H}_y}}{\mathrm{N_A}}\frac{1}{h} \tag{2}$$

where $\mathrm{N_A}$ is Avogadro's constant. The density of the amorphous sub-stoichiometric film grown at 100°C is about 3.0 g.cm^{-3}, significantly lower than the standard density of anatase TiO$_2$ (3.78 g. cm^{-3}). This suggests that the film is porous. In contrast the calculated density of the crystalline film grown at 225°C (in the so-called ALD window) is ~ 3.64 g.cm^{-3} which is close to that of anatase TiO$_2$. Consequently the "225°C" film is more compact than that grown at 100°C. This is consistent with the GIXRD data which show the typical anatase diffraction peaks. The calculated density of the 300°C film is ~3.85 g.cm^{-3}, bracketed by that of anatase and that of

rutile (4.23 g.cm^{-3}). This is also consistent with the GIXRD data that indicate a mixture of both phases.

The XPS core-level (Figures 4 and 5) and valence band (Figure 6) spectra give crucial information on the electronic structure of the films. However, as the films were prepared ex-situ and transported in air, the C 1s and O 1s levels are inevitably affected by surface contamination (water, organics). C 1s and O 1s spectra are presented in the supplementary material, in section S1 (Figure S1) and section S2 (Figure S2), respectively. The O 1s spectra are characterized by a main component attributed to bulk O^{2-} at around 530.5 eV, with a spectral weight of 82-83 %. Higher BE components are found at ~531.6 eV (ΔBE=1.1 eV with respect to O^{2-}) and in the 532.8-532.9 eV (ΔBE=2.3-2.4 eV with respect to O^{2-}) range (the fitting parameters are given in Table S2). These components can be attributed to hydroxyls, and to O-containing organic species, in particular carboxylic acids or esters (that appear with a C 1s component at 289.3 eV, see Figure S1 of the supplementary material). Independently of surface contamination, the BE of the main O^{2-} component of the as-grown samples, reported in Table 3, is a characteristic proxy of the material, helpful for comparison with other TiO$_2$ crystalline surfaces (anatase and rutile).[24] We can calculate the stoichiometric ratio $\left(\frac{n_O}{n_{Ti}}\right)^{XPS}$ where n_O and n_{Ti} are the number of oxygen atoms and titanium atoms per unit volume from the O 1s intensity I$_{O\ 1s}$ and that of the Ti 2p spectrum I$_{Ti\ 2p}$. The method and the calculated $\left(\frac{n_O}{n_{Ti}}\right)^{XPS}$ values are reported in section S3 of the supplementary material (Table S3). These values depend on calculated inelastic mean free paths and atomic photo-ionization cross-sections. Considering the total O 1s intensity, $\left(\frac{n_O}{n_{Ti}}\right)^{XPS}$ is in the range 2.4±0.1 for all three temperatures (diminishing to 1.99±0.04 considering only the O^{2-} intensity). This XPS result concerns only the outer few nm of the film, and can be contrasted with the IBA results which give a composition averaged over the entire film thickness.

As discussed above, the nitrogen is not detected by NRA. However, the N 1s peaks are invariably observed in the XPS surveys, for all growth temperatures. They are displayed in Figure 4. The N 1s normalized intensity is defined as the $\frac{I_{N\,1s}}{I_{Ti\,2p}}$ ratio, where $I_{N\,1s}$ and $I_{Ti\,2p}$ are the intensities of the N 1s signal and Ti 2p signal, respectively (the $\frac{I_{N\,1s}}{I_{Ti\,2p}}$ values are reported in Figure 4). For the depositions at 100°C and 225°C, $\frac{I_{N\,1s}}{I_{Ti\,2p}}$ does not change much, remaining at ~2%. Nitrogen is still detected for the 300°C film, as $\frac{I_{N\,1s}}{I_{Ti\,2p}} \sim 0.7\%$ (smaller by a factor of 3). These findings are comparable to those of Saari et al.[5] who obtained $\frac{I_{N\,1s}}{I_{Ti\,2p}}$ ratios of ~2% (100°C) and ~0.7% (200°C). From the XPS $\frac{I_{N\,1s}}{I_{Ti\,2p}}$ ratios and assuming all the nitrogen atoms to be on the surface, we have estimated the surface density of nitrogen atoms (supplementary material, section S4, Table S4) to be in the range 2×10^{14} cm^{-2} (300°C) to 6×10^{14} cm^{-2} (100°C-225°C) for the as grown samples. The Ar bombardment of the "100°C" sample (that sputters a few monolayers of the material) diminishes the nitrogen N 1s signal by a factor of 2. The effect of sputtering is even stronger for the "225°C" sample as $\frac{I_{N\,1s}}{I_{Ti\,2p}}$ decreases from 2% to 0.25%. This is indicative that the nitrogen species tend to dwell at the surface. Since α particles from ^{14}N(d,α$_0$)^{12}C and ^{14}N(d,α$_1$)^{12}C nuclear reactions are not detected, we propose that the deuteron beam stimulates the desorption of nitrogen containing surface species during NRA measurements.

Sample	100°C BE (eV)	225°C BE (eV)	300°C BE (eV)	Poly-anatase Stoichiometric (*) Water-exposed (♥) BE (eV)
(O^{2-}) O 1s	530.61	530.47	530.46	530.35*/530.64♥
N 1s				
N1	402.12 (54.1)	402.15 (18.5)	401.80 (16.0)	
N2	400.42 (42.4)	400.56 (70.8)	400.48 (68.5)	
N3	399.20 (3.5)	399.1 (10.7)	399.16 (15.5)	
Ti 2p$_{3/2}$				
Ti^{4+}	459.12 (98.3)	459.26 (100)	459.29 (100)	459.06*/459.37♥
Ti^{3+}	457.55 (1.7)	no	no	
Valence				
GS	1.08	no	no	-
VBE	3.60	3.44	3.48	3.12*/3.31♥

Table 3. Binding energy (BE) of the fitting components and spectral weights (%) of the Ti 2p, valence band, O 1s and N 1s core-level spectra. Binding energy position of the valence band edge (VBE) and gap state centroid (GS). Data from UHV stoichiometric and water-exposed stoichiometric polycrystalline anatase (poly-anatase) from ref [24] are also given for comparison.
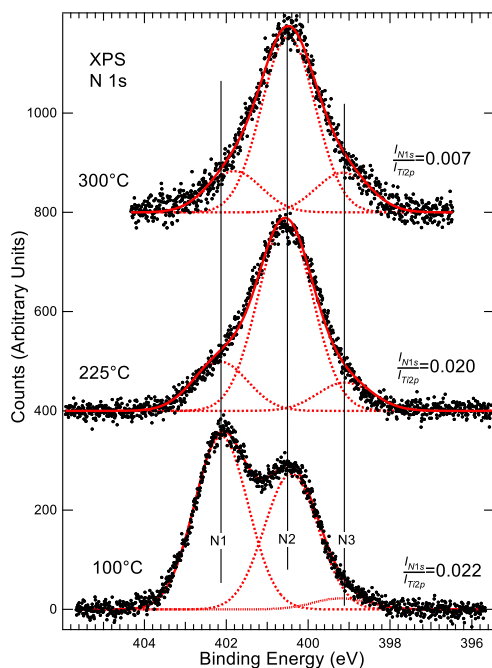
Figure 4. The N 1s core-level (hν=1487.1 eV) measured with a monochromatized Al Kα source for the films produced at 100°C, at 225 °C, and at 300°C. The peak is fitted with Gaussians of FWHM equal to 1.56 eV. A Shirley background[47] is subtracted. The $\frac{I_{N\,1s}}{I_{Ti\,2p}}$ ratio is given for each spectrum. N1 is attributed to DMAH$^+$, N2 to adsorbed DMA, N3 to the amido ligand (or possibly to adsorbed Me-N=CH$_2$).

As already pointed out by Head et al.[17] the N 1s spectra give crucial information on the "ideality" of the ALD process. We recall that the last half-cycle was a water exposure followed by a N_2 purge. The N 1s spectra of the "as-grown" samples shown in Figure 4 are fitted with only 3 components: N1 in the range 401.8-402.2 eV, N2 at ~400.4-400.6 eV, and N3 at ~399.1 eV. These same three components are also observed in the N 1s spectra of Saari et al..[5] In refs [5] and [17] the N3 component is attributed the amido component, i.e. unreacted Ti-N(Me)$_2$ bonds due to incomplete TDMAT dissociation. However, we note that the BE of adsorbed imines is expected at 398.4 eV,[48][49] which means that their presence cannot be completely excluded. Whatever the attribution of N3, its contribution is always minor (Figure 4). For the attributions of the components N1 and N2, we follow those given in refs[5] and [17]. Both N1 and N2 are related to adsorbed DMA, the byproduct of the ligand exchange reactions R1 and R2. N2 is associated to DMA datively bonded to the undercoordinated Ti_{5c} Lewis acidic sites (the five-coordinated Ti_{5c} $Ti^{4+}$is present on anatase and rutile surfaces, together with the bridging two-coordinated oxygen O_{2c}). Indeed, the dative bonding of ammonia/amines on dehydrated (101) anatase is characterized by N 1s BEs ranging from 400.1 eV (ammonia), 400.6 eV (ethylamine) and 401.1 eV (DMA).[50] Similarly, methylamine is bound on the Ti_{5c} sites of rutile (110) with a N 1s BE of 400.8 eV.[51] The measured desorption energy of methylamine on dehydrated rutile (110) ranges from ~1eV (DFT-modeling by a unidentate dative bonding with Ti_{5c}) to 1.53 eV (DFT-modeling by a multidentate site, i.e. dative bonding with one Ti_{5c} plus H bonds with neighboring oxygens).[51] Calculations give a "single head" adsorption energy of ~2 eV for ethylenediamine on dehydrated (101) anatase[52] which adopts a multidentate geometry. Relatively large adsorption values would imply that the N2/DMA species could remain adsorbed on the surface still after a purge at 300°C (573 K). For its part, N1 can be attributed to dimethylammonium (DMAH$^+$) resulting from a reaction of DMA with

a Brønsted acidic hydroxyl. Indeed, ammonia is protonated on hydrated rutile, with a high N 1s BE for NH_4^+.[53] During the ALD growth of TiO_2, two types of hydroxyls with two different $\nu(OH)$ bands are detected by infrared spectroscopy. The band at (3660-3685) cm^{-1} is attributed to bridging OH (H$^+$ +O$_{2c}$), while the one at 3700 cm^{-1} is associated to terminal OH (HO$^-$Ti$_{5c}$) respectively.[19] Bridging OH are considered to be acidic on (101) anatase.[54] It is clear from Figure 4 that the N1/N2 intensity ratio is much greater for the "100°C" film than for the films made at higher temperature. This same trend was also observed by Saari et al..[5] The predominance of the N1 (DMAH$^+$) species on the "100°C" oxide suggests there are more acidic bridging OHs than in the case of films made at higher temperature. Head et al..[17] also observed the components N1, N2 and N3, but in contrast to Saari et al. and the present study, they saw a fourth component at ~397.0 eV, which they attributed to the Ti-C-N metallacycle (see Figure 1(c), left scheme). This is a plausible attribution considering the β-elimination decomposition mechanisms that were calculated for gas phase TMDAT. If the Ti-C-N metallacycle compound were ever produced in the present conditions, the N 1s spectra clearly show it cannot stay on the surface. The discrepancy between our findings and the in-situ study of Head et al.[17] can be explained by different experimental conditions. First, Head et al. focused on the growth of the very first layers (the three first cycles). The composition of the ultrathin titanium oxide layer may have a role in forming or retaining the Ti-C-N metallacycle (this was already suggested by Sperling et al.[19]). Second, the water exposure during the film growth in the present work can be more effective to eliminate the Ti-C-N metallacycle (possibly via a hydrolyzation step followed by desorption).

The N 1s spectra confronted to the IBA results can also give hints on the chemical nature of hydrogen embedded in the films. The high H bulk content (especially for the "100°C" growth) *cannot* be linked to the reaction byproducts DMA (N2) and DMAH$^+$ (N1) that are necessarily confined at the oxide surface. On the other hand, H can be provided by water (Ti-

OH left unreacted after TDMAT half-cycles, embedded water molecules). It can also result

from the β-elimination channel (in the gas phase or at the surface, Figure 1 (b,c)) that leads to

Ti-H *plus* an N-methylmethyleneimine molecule escaping into the gas phase (if the imine

adsorbs it may contribute to N3 in Figure 4). Isotopic tracing experiments using D_2O could

reveal the hydrogen source.
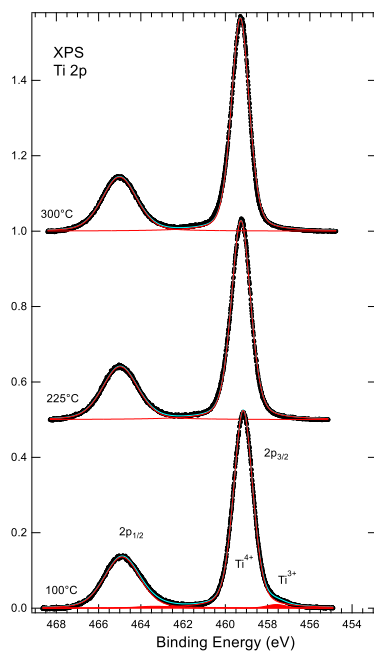
Figure 5. Ti 2p spectra obtained with a monochromatized Al K$_\alpha$ source from TiO$_2$ layers produced at 100°C, 225°C, and 300°C. A Shirley background[47] is subtracted. The spectra are normalized to identical areas. Fits of the experimental curves are made with sums of pseudo-Voigt functions. The FWHM (Gaussian fraction) is 1.083 eV (0.68) for Ti 2p$_{3/2}$ and 1.980 eV (0.75) for Ti 2p$_{1/2}$. Note the very small Ti^{3+} component of the "100°C" sample (Ti^{3+}/(Ti^{3+} + Ti^{4+}) ~1.7%).
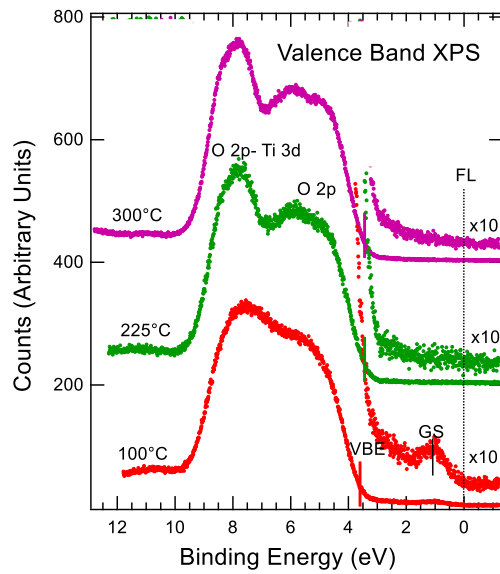
Figure 6. Valence band spectra of the TiO_2 layers produced with a monochromatized Al K_α source for the 100°C, 225°C, and 300°C films. No background is subtracted. The valence band edge (VBE) is indicated by a colored vertical bar, and the Fermi level (FL) by a vertical dashed dark line. In the layer produced at 100°C, notice the presence of a tail extending from VBE and a gap state (GS) centered at 1.1 eV. Gap states are not detected for samples produced at 225°C and 300°C.

The Ti 2p and valence band spectra, given in Figure 5 and 6, respectively, are discussed together as they both give information on the reduction state of the oxide. The Ti 2p core-level is actually a doublet (Ti $2p_{3/2}$ and Ti $2p_{1/2}$) separated by a spin-orbit splitting of 5.72 eV. The spectra are fitted with symmetric pseudo-Voigt components (a pseudo-Voigt function is a weighted sum of a Gaussian and a Lorentzian that simulates a Voigt function). For the pseudo-Voigt components fitting the Ti $2p_{3/2}$ peak, the Gaussian fraction is 67.8% and the FWHM is 1.08 eV. For the broader pseudo-Voigt components fitting the Ti $2p_{1/2}$ peak, the Gaussian fraction is 74.6% and the FWHM is 1.21 eV. In the 100°C-300°C window, the FWHM of the Ti $2p_{3/2}$ component (1.08 eV) is not affected by the deposition temperature. This means that the Ti 2p core level is essentially influenced by local order, as the 100°C sample is amorphous, while the "225°C" and "300°C" samples are microcrystalline. This contrasts with the valence band spectra whose shape changes with deposition temperature and an increased crystallinity. In anatase[55] and rutile[56] the calculated projected density of state (DOS) shows that the contribution of the O 2p level is dominant from the valence band edge (VBE) and ~3 eV below. Lower-lying energy valence band levels are a mixture of Ti 3d and O 2p levels. At hv=1486.71 eV, the O 2p and Ti 3d photoionisation cross-sections of 2.602 10^{-4} and 1.894 10^{-4} Mbarn respectively are comparable.[34] The valence band consists of two broad structures. These are related to the O 2p (~5 eV) and mixed Ti 3d-O 2p levels (~7.5 eV) as may be seen in Figure 5. The VBE is determined as the intersection of the tangent at the inflection point of the low BE O 2p flank with the horizontal baseline (the method is illustrated in the SI, section S6, Figure S4). The VBE positions are indicated by vertical bars (the values are also given in Table 3). To help interpreting the VBE position with respect to the Fermi level, we recall that the band gaps of the low temperature crystalline phase (anatase) are 3.23 eV (indirect gap) and 3.8 eV (direct gap).[57] The smaller direct and indirect gaps of rutile are ~3.0 eV.[58] The BEs of Ti $2p_{3/2}$ peak and VBE are collected in Table 3. An in-depth analysis of the titanium oxidation state was

not possible using layer-by-layer sputtering of the oxide with Ar bombardment, because this commonly used technique led to strong O losses and hence reduction of the oxide (see supplementary material, section S7).

For the amorphous "100°C" sample, an accurate fit of the Ti 2p spectrum (Figure 5) needs the introduction of a weak component shifted to a BE (-1.57 eV) lower than the main Ti $2p_{3/2}$ peak at 459.12 eV characteristic of Ti^{4+}.[24] The low BE peak is attributed to the Ti^{3+} state. In the valence band spectrum (Figure 6) VBE is at a BE of 3.60 eV. Given the band gap values of the crystalline polymorphs (3.0-3.3 eV), we can assume that the Fermi level is aligned with the bottom of the conduction band. We see a "tail" of occupied states extending from VBE. In the oxide gap, a peak (denoted GS) is observed centered at ~1.1 eV below the Fermi level. The gap state peak intensity is also rather weak, about 0.5% of the total valence band signal integrated from the Fermi level to 10 eV below, which is consistent with the Ti^{3+} intensity in the Ti 2p spectrum ($Ti^{3+}/(Ti^{3+} + Ti^{4+}) = 1.7\%$). Note that the *deep* gap states of Figure 6 are different from the *shallow* gap states that result from creating O vacancies under Ar bombardment. In fact, these defects extend from the Fermi level: the Ar-etched spectrum of the 225°C (anatase) sample shown in Figure S6, section S7 of the supplementary material, presents a marked Fermi edge.

To sum up, from the point of view of XPS, the oxidation state of titanium in "100°C" film is essentially Ti^{4+}, while IBA points to an O-deficient ($[^{16}O]/[Ti]\sim1.8$) and H-rich film ($[^{1}H]/[Ti]\sim0.5$). Both latter two observations should strongly impact the electronic structure, which is apparently not the case. To reconcile the IBA and XPS results, one must recall that XPS is sensitive to the outermost few nm of the material. This would mean that the XPS-probed layers of the "100°C" sample are much less reduced than the inner ones. However, the complexity of the electronic structure of a reduceable cation oxide like titania and the presence

of large impurity contents (H) deserves much more attention than a mere statement on depth inhomogeneity.

Calculations show that O vacancies (point defects) create gap states.[22] Once one O vacancy is created, two electrons are transferred to two Ti^{4+} to give two Ti^{3+} states (with one unpaired electron $3d^1$ on each atom). Gap states are also related to the presence of impurity atoms, and H is particularly abundant in the "100°C" sample. According to GGA-U calculations, an interstitial hydrogen in TiO_2 bonds like a proton H^+ to an O^{2-} ion (to produce an HO^-) and the released electron occupies a 3d state ($3d^1$).[23] Assuming that a mixed oxide/hydroxide is formed with a stoichiometry $Ti^{4+}_{1-x}Ti^{3+}_x O^{2-}_{2-x}(OH)^-_x$, then the ratio $Ti^{3+}/(Ti^{3+} + Ti^{4+})$ should also be x. Therefore, one should expect a very large Ti^{3+} intensity in the Ti 2p and valence bands, which is not the case. However, H atoms may exist not as interstitials, but rather as H atoms trapped into O vacancies, [59]'[60] where they are much more tightly bound. We note that given the growth temperatures, the assumption of H interstitials is not realistic[59]. H at a neutral oxygen vacancy site is negatively charged according to calculations: hydrides are formed [59] and up to two atoms can be trapped.[60] The trapped atoms may siphon the charge of the occupied 3d level resulting from O vacancy formation, which would explain the small concentration of Ti^{3+} states seen by XPS. The high H content of the "100°C" sample and its amorphous nature, remind us of black amorphous $H-TiO_2$. For this material, the Ti 2p XPS spectra given by Chen et al.[61] show no Ti^{3+} states. However, gap states extend from the top of the valence band, reducing the gap width, [61] similar to the "tailing" seen above the VBE in Figure 6. This is a further indication that high H contents do not necessarily imply the reduction of Ti^{4+} to Ti^{3+}.

For the "crystalline" samples grown at 225°C and 300°C, the Ti 2p spectra (Figure 5) indicate that the oxidation state is 100% Ti^{4+}. We recall that the $[^{16}O]/[Ti]$ ratio of 2 fits within the measurement interval of IBA. However, ERDA still detects substantial hydrogen atoms in

the crystalline films that have average stoichiometries $TiO_2H_{0.12}$ and $TiO_2H_{0.07}$ when grown at 225°C and 300°C, respectively. As discussed above, the presence of hydrogen does not necessarily imply the presence of Ti^{3+}, and we may imagine crystallites whose core is crystalline with a thin H-rich and disordered external layer, as is the case for amorphous $H-TiO_2$.[61] The valence band spectra (Figure 6) are markedly different from that of the amorphous "100°C" sample. In particular the dip between the "mixed O 2p-Ti 3d" and "O 2p" bands is much more pronounced. This feature is clearly associated with crystallographic ordering. The VBE are found at 3.44 eV ("225°C") and 3.48 eV ("300°C"), values smaller than that of the "100°C" film. Given the VBE position, and band gaps in the 3.0-3.3 eV range for anatase and rutile, we can consider that the Fermi level lies close to the conduction band (see below). We see no gap states in the valence band. Looking to the XPS proxies, that is Ti $2p_{3/2}$, (O^{2-}) O 1s and VBE energy positions of the "225°C and 300°C" samples, we can verify (Table 4) that they are closer to the values reported by Kashiwaya et al.[24] for the water-exposed stoichiometric polycrystalline anatase, than to those of the same "dry" UHV surface. As discussed by Kashiwaya et al. water adsorption leads to an increase in BE, which is interpreted as a downward band bending leading to an accumulation layer at the oxide surface. This can be considered as an *a posteriori* justification of our assumption concerning the positioning of the Fermi level at the conduction band minimum.

The present study illustrates that the TiO_2 ALD deposition conditions have a strong impact on the nature of the grown layers. In particular, the equal half-cycle time lengths for the metallic precursor and oxidant used here have resulted in quite different film properties to those obtained with very different half-cycle times. Indeed, Saari et al..[5] used the TDMAT/water couple in the 100°C-200°C window to produce amorphous films. While in both works, the TDMAT pulse durations are comparable, 1.6 s in Saari et al. [5] and 1.5 s here, the water pulse was only 0.1 s in Saari et al. and is 2 s in the present case. These authors characterized their

films with monochromatized Al K$_\alpha$ XPS as we did, but they did not measure the H-content in the oxide. They observed that the Ti^{3+} weight in the Ti 2p spectrum is already substantial in the amorphous film made at 100°C (11%), and that it increases with temperature, reaching 30% at 200°C. This temperature trend is not seen here, and the Ti^{3+} weight does not exceed 1.7% for the "100°C" sample, and is null for higher growth temperatures. The gap states are also different in ref[5]. Shallow gap states are observed at the Fermi level, similar to the O-deficient Ar-bombarded anatase film reported in section S7, Figure S6 of the supplementary material. We propose that long oxidant half-cycles produce films with the highest oxidation state of the cation. The comparison of the present experiment with that of Saari et al. emphasizes the "versatility" of titania ALD deposition using the TMDAT/water couple. It is clear that the oxygen deficiency, H content and Ti oxidation state, that are of paramount importance to define the electronic structure (conductivity and optical properties) and network structure (order, defects etc.) can be tuned with temperature and water exposure times.

CONCLUSIONS

Ion Beam Analysis and monochromatized X-ray photoemission spectroscopy were used in combination to characterize titanium dioxide thin (~11 nm) films produced by ALD in conditions where the TMDAT and water exposures have comparable time lengths. Ancillary techniques like X-ray diffraction and ellipsometry were also used to determine the crystallography and film thickness, respectively. IBA and XPS enabled us to characterize the material from different viewing angles, as IBA counts all atoms (Ti, O, N, H) comprised in a unit area of the oxide film and gives access to "in-depth" atomic profiles (H), while XPS is a surface technique sensitive to the chemical bond and the band structure. Nitrogen is not detected by IBA, but protonated and unprotonated DMA molecules are seen by XPS at the oxide surface. This observation enters into the picture of ligand exchange reactions, as the DMA molecule is

the expected by-product. Concerning the self-dissociation of TMDAT in the gas phase or at the surface, that would compete with the ligand exchange reaction, we see no Ti-C-N metallacycle moieties on the surface, in contrast with a previous in-situ NAP-XPS study. As the DMA molecules are confined to the surface, they cannot be the source of the H-content detected by IBA in the films. This a unique deduction from the combination of IBA and XPS techniques.

The amorphous films, produced at the lowest temperature of 100°C, are less dense than the crystalline forms of TiO_2 and defective. IBA shows that they are sub-stoichiometric in oxygen ([O]/[Ti]=1.80±0.08) and hydrogen-rich ([H]/[Ti]~0.5). For its part, XPS indicates that in the outermost layers (several nanometers) probed by the technique the titanium cations are essentially (98.3%) in the Ti^{4+} state. The valence band edge binding energy suggests that the Fermi level is close to the conduction band (*n*-type sample). A tail of states extends from the valence band edge into the gap, and a (weak intensity) gap state level is seen peaked at 1.1 eV from the Fermi level (likely a Ti^{3+} $3d^1$ state). Consequently, the large O-deficiency and high H-content are expected to yield a considerably higher content of reduced Ti^{3+} state than that actually observed by photoemission. We discuss this point, considering the theoretical literature on defects in crystalline titania forms, and emphasize similarities with amorphous $H-TiO_2$ for which no correlation between H content and reduction of Ti^{4+} to Ti^{3+} has been observed.

In contrast to the "100°C" sample, films grown in the so-called ALD window (225°C) and above (300°C) are crystalline (anatase at 225°C, anatase *plus* rutile at 300°C) and have densities close to those of the crystalline phases. An [O]/[Ti] ratio of 2 is within the error bars of the IBA measurements. Only Ti^{4+} states are seen in the XPS Ti 2p levels, and no gap states are found in the valence band spectra. The binding energy of the valence band edge shows that the films are *n*-type. The H content given by ERDA, although substantially reduced with respect to the "100°C" sample, remains significant with [H]/[Ti] in the 10 at% range. The absence of

reduced Ti^{3+} states in the core and valence XPS spectra suggests again that the hydrogen content does not correlate with the reduction of Ti^{4+} to Ti^{3+}.

The TDMAT/water couple and the growth temperature do not define alone the outcomes of the ALD process. By adopting water half-cycle times as long as those of the TDMAT, we have deposited film with Ti ions almost exclusively in the Ti^{4+} state in the 100°C-300°C range, but with substantial variations in the O and H content. The comparison of the present experiment with the recent work of Saari et al.[5] emphasizes that the composition, electronic and network structure can be tuned in a wide range thanks to the "versatility" of the ALD deposition process, which paves the way to applications where conductive films with Ti in its highest oxidation state is an advantage, for instance in electron storage materials.

CRediT author statement

B. Xia: Conceptualization (ALD, IBA), Methodology, Investigation, Writing.

JJ Ganem: Conceptualisation (ALD, IBA), Methodology, Validation, Writing – review & editing.

I. Vickridge: Writing – review & editing.

Emrick Briand: Investigation (IBA)

Sébastien Steydli: Investigation (IBA)

Rabah Benbalagh: Methodology (XPS), Investigation (XPS), Validation (XPS).

François Rochet: Conceptualization (XPS), Methodology (XPS), Validation (XPS), Writing – original draft.

Declaration of Competing Interest

The authors declare that they have no known competing financial interests or personal relationships that could have appeared to influence the work reported in this paper.

Acknowledgements

Appendix A. Supplementary material

Supplementary data to this article can be found online

References

[1]   A.L. Linsebigler, G. Lu, J.T. Yates, Photocatalysis on TiO2 Surfaces: Principles, Mechanisms, and Selected Results, Chem. Rev. 95 (1995) 735–758. https://doi.org/10.1021/cr00035a013.

[2]   V. Pore, T. Kivelä, M. Ritala, M. Leskelä, Atomic layer deposition of photocatalytic TiO2 thin films from TiF4 and H2O, Dalt. Trans. (2008) 6467–6474. https://doi.org/10.1039/B809953G.

[3]   P.J. Barczuk, K.R. Noworyta, M. Dolata, K. Jakubow-Piotrowska, J. Augustynski, Visible-light activation of low-cost rutile TiO2 photoanodes for photoelectrochemical water splitting, Sol. Energy Mater. Sol. Cells. 208 (2020) 110424. https://doi.org/10.1016/j.solmat.2020.110424.

[4]   P. Nunez, M.H. Richter, B.D. Piercy, C.W. Roske, M. Cabán-Acevedo, M.D. Losego, S.J. Konezny, D.J. Fermin, S. Hu, B.S. Brunschwig, N.S. Lewis, Characterization of Electronic Transport through Amorphous TiO 2 Produced by Atomic Layer Deposition, J. Phys. Chem. C. 123 (2019) 20116–20129. https://doi.org/10.1021/acs.jpcc.9b04434.

[5]   J. Saari, H. Ali-Löytty, M.M. Kauppinen, M. Hannula, R. Khan, K. Lahtonen, L. Palmolahti, A. Tukiainen, H. Grönbeck, N. V. Tkachenko, M. Valden, Tunable Ti 3+ - Mediated Charge Carrier Dynamics of Atomic Layer Deposition-Grown Amorphous TiO 2, J. Phys. Chem. C. (2022) acs.jpcc.1c10919. https://doi.org/10.1021/acs.jpcc.1c10919.

[6]   Y.-S. Kim, K.D. Harris, B. Limoges, V. Balland, On the unsuspected role of multivalent metal ions on the charge storage of a metal oxide electrode in mild aqueous electrolytes, Chem. Sci. 10 (2019) 8752–8763. https://doi.org/10.1039/C9SC02397F.

[7]   Y.-Q. Cao, S.-S. Wang, C. Liu, D. Wu, A.-D. Li, Atomic layer deposition of ZnO/TiO2 nanolaminates as ultra-long life anode material for lithium-ion batteries, Sci. Rep. 9

(2019) 11526. https://doi.org/10.1038/s41598-019-48088-2.

[8]   C. Geng, T. Sun, Z. Wang, J.-M. Wu, Y.-J. Gu, H. Kobayashi, P. Yang, J. Hai, W. Wen, Surface-Induced Desolvation of Hydronium Ion Enables Anatase TiO 2 as an Efficient Anode for Proton Batteries, Nano Lett. 21 (2021) 7021–7029. https://doi.org/10.1021/acs.nanolett.1c02421.

[9]   N. Makivić, J.-Y. Cho, K.D. Harris, J.-M. Tarascon, B. Limoges, V. Balland, Evidence of Bulk Proton Insertion in Nanostructured Anatase and Amorphous TiO 2 Electrodes, Chem. Mater. 33 (2021) 3436–3448. https://doi.org/10.1021/acs.chemmater.1c00840.

[10]   Y. Cao, X. Meng, A. Li, Atomic Layer Deposition of High-Capacity Anodes for Next-Generation Lithium-Ion Batteries and Beyond, ENERGY Environ. Mater. 4 (2021) 363–391. https://doi.org/10.1002/eem2.12132.

[11]   S. Liang, X. Wang, Y.-J. Cheng, Y. Xia, P. Müller-Buschbaum, Anatase titanium dioxide as rechargeable ion battery electrode - A chronological review, Energy Storage Mater. 45 (2022) 201–264. https://doi.org/10.1016/j.ensm.2021.11.023.

[12]   J.-P. Niemelä, G. Marin, M. Karppinen, Titanium dioxide thin films by atomic layer deposition: a review, Semicond. Sci. Technol. 32 (2017) 93005. https://doi.org/10.1088/1361-6641/aa78ce.

[13]   W.J. Maeng, H. Kim, Thermal and Plasma-Enhanced ALD of Ta and Ti Oxide Thin Films from Alkylamide Precursors, Electrochem. Solid-State Lett. 9 (2006) G191. https://doi.org/10.1149/1.2186427.

[14]   J.-Y. Yun, M.-Y. Park, S.-W. Rhee, Comparison of Tetrakis(dimethylamido)titanium and Tetrakis(diethylamido)titanium as Precursors for Metallorganic Chemical Vapor Deposition of Titanium Nitride, J. Electrochem. Soc. 146 (1999) 1804–1808. https://doi.org/10.1149/1.1391847.

[15]   E.T. Norton, C. Amato-Wierda, Kinetic and Mechanistic Studies of the Thermal

Decomposition of Ti(N(CH 3) 2) 4 during Chemical Vapor Deposition by in Situ Molecular Beam Mass Spectrometry, Chem. Mater. 13 (2001) 4655–4660. https://doi.org/10.1021/cm0104708.

[16] K. Sen, T. Banu, T. Debnath, D. Ghosh, A.K. Das, Towards a comprehensive understanding of the chemical vapor deposition of titanium nitride using Ti(NMe2)4: a density functional theory approach, Dalt. Trans. 43 (2014) 8877. https://doi.org/10.1039/c4dt00690a.

[17] A.R. Head, S. Chaudhary, G. Olivieri, F. Bournel, J.N. Andersen, F. Rochet, J.-J. Gallet, J. Schnadt, Near Ambient Pressure X-ray Photoelectron Spectroscopy Study of the Atomic Layer Deposition of TiO 2 on RuO 2 (110), J. Phys. Chem. C. 120 (2016) 243–251. https://doi.org/10.1021/acs.jpcc.5b08699.

[18] P. Shayesteh, R. Tsyshevsky, S. Urpelainen, F. Rochet, F. Bournel, J.-J. Gallet, M.M. Kuklja, J. Schnadt, A.R. Head, Experimental and theoretical gas phase electronic structure study of tetrakis(dimethylamino) complexes of Ti(IV) and Hf(IV), J. Electron Spectros. Relat. Phenomena. 234 (2019). https://doi.org/10.1016/j.elspec.2019.05.016.

[19] B.A. Sperling, J. Hoang, W.A. Kimes, J.E. Maslar, K.L. Steffens, N. V. Nguyen, Time-resolved surface infrared spectroscopy during atomic layer deposition of TiO 2 using tetrakis(dimethylamido)titanium and water, J. Vac. Sci. Technol. A Vacuum, Surfaces, Film. 32 (2014) 031513. https://doi.org/10.1116/1.4872166.

[20] K. Xu, A.P. Milanov, H. Parala, C. Wenger, C. Baristiran-Kaynak, K. Lakribssi, T. Toader, C. Bock, D. Rogalla, H.-W. Becker, U. Kunze, A. Devi, Atomic Layer Deposition of HfO2 Thin Films Employing a Heteroleptic Hafnium Precursor, Chem. Vap. Depos. 18 (2012) 27–35. https://doi.org/10.1002/cvde.201106934.

[21] K. Kukli, M. Ritala, T. Sajavaara, J. Keinonen, M. Leskelä, Atomic Layer Deposition of Hafnium Dioxide Films from Hafnium Tetrakis(ethylmethylamide) and Water, Chem.

Vap.   Depos.   8   (2002)   199–204.   https://doi.org/10.1002/1521-3862(20020903)8:5<199::AID-CVDE199>3.0.CO;2-U.

[22]   C. Di Valentin, G. Pacchioni, A. Selloni, Reduced and n-Type Doped TiO 2 : Nature of Ti 3+ Species, J. Phys. Chem. C. 113 (2009) 20543–20552. https://doi.org/10.1021/jp9061797.

[23]   M.M. Islam, M. Calatayud, G. Pacchioni, Hydrogen Adsorption and Diffusion on the Anatase TiO 2 (101) Surface: A First-Principles Investigation, J. Phys. Chem. C. 115 (2011) 6809–6814. https://doi.org/10.1021/jp200408v.

[24]   S. Kashiwaya, J. Morasch, V. Streibel, T. Toupance, W. Jaegermann, A. Klein, The Work Function of TiO2, Surfaces. 1 (2018) 73–89. https://doi.org/10.3390/surfaces1010007.

[25]   P. Reckers, M. Dimamay, J. Klett, S. Trost, K. Zilberberg, T. Riedl, B.A. Parkinson, J. Brötz, W. Jaegermann, T. Mayer, Deep and Shallow TiO 2 Gap States on Cleaved Anatase Single Crystal (101) Surfaces, Nanocrystalline Anatase Films, and ALD Titania Ante and Post Annealing, J. Phys. Chem. C. 119 (2015) 9890–9898. https://doi.org/10.1021/acs.jpcc.5b01264.

[26]   C. Di Valentin, G. Pacchioni, Spectroscopic Properties of Doped and Defective Semiconducting Oxides from Hybrid Density Functional Calculations, Acc. Chem. Res. 47 (2014) 3233–3241. https://doi.org/10.1021/ar4002944.

[27]   FilmSenceLLC, FS-1 manual 2020, (n.d.).

[28]   J.A. Davies, T.E. Jackman, H.L. Eschbach, W. Dobma, U. Wätjen, D. Chivers, Calibration of the Harwell series II Bi-implanted RBS standards, Nucl. Instruments Methods Phys. Res. Sect. B Beam Interact. with Mater. Atoms. 15 (1986) 238–240. https://doi.org/10.1016/0168-583X(86)90293-4.

[29]   L. Lemelle, F. Abel, C. Cohen, F. Guyot, Study of the (010) olivine surface by

Rutherford backscattering spectrometry in channeling geometry, Am. Mineral. 87 (2002) 327–332. https://doi.org/10.2138/am-2002-2-315.

[30] J.-J. Ganem, S. Rigo, I. Trimaille, G.-N. Lu, NRA characterization of pretreatment operations of silicon, Nucl. Instruments Methods Phys. Res. Sect. B Beam Interact. with Mater. Atoms. 64 (1992) 784–788. https://doi.org/10.1016/0168-583X(92)95578-F.

[31] S. Rigo, G. Amsel, M. Croset, Investigation of reactively sputtered silicon nitride films by complementary use of backscattering and nuclear-reaction microanalysis results, J. Appl. Phys. 47 (1976) 2800–2810. https://doi.org/10.1063/1.323076.

[32] M. Mayer, SIMNRA, a simulation program for the analysis of NRA, RBS and ERDA, in: AIP Conf. Proc., AIP, 1999: pp. 541–544. https://doi.org/10.1063/1.59188.

[33] J.F. Ziegler, G.W. Cole, J.E.E. Baglin, Technique for determining concentration profiles of boron impurities in substrates, J. Appl. Phys. 43 (1972) 3809–3815. https://doi.org/10.1063/1.1661816.

[34] J.J. Yeh, I. Lindau, Atomic Subshell Photoionization Cross Sections and Asymmetry Parameters: 1 < Z <103, At. Data Nucl. Data Tables. 32 (1985) 1–155.

[35] C.J. Powell, A. Jablonski, NIST Electron Inelastic-Mean-Free-Path Database, NIST Standard Reference Database 71 version 1.2, Gaithersburg. (2010).

[36] J. Aarik, A. Aidla, T. Uustare, V. Sammelselg, Morphology and structure of TiO2 thin films grown by atomic layer deposition, J. Cryst. Growth. 148 (1995) 268–275. https://doi.org/10.1016/0022-0248(94)00874-4.

[37] M. Reiners, K. Xu, N. Aslam, A. Devi, R. Waser, S. Hoffmann-Eifert, Growth and Crystallization of TiO 2 Thin Films by Atomic Layer Deposition Using a Novel Amido Guanidinate Titanium Source and Tetrakis-dimethylamido-titanium, Chem. Mater. 25 (2013) 2934–2943. https://doi.org/10.1021/cm303703r.

[38] A. Chaker, P.D. Szkutnik, J. Pointet, P. Gonon, C. Vallée, A. Bsiesy, Understanding the

mechanisms of interfacial reactions during TiO 2 layer growth on RuO 2 by atomic layer deposition with O 2 plasma or H 2 O as oxygen source, J. Appl. Phys. 120 (2016) 085315. https://doi.org/10.1063/1.4960139.

[39] S. Zhuiykov, M.K. Akbari, Z. Hai, C. Xue, H. Xu, L. Hyde, Wafer-scale fabrication of conformal atomic-layered TiO2 by atomic layer deposition using tetrakis (dimethylamino) titanium and H2O precursors, Mater. Des. 120 (2017) 99–108. https://doi.org/10.1016/j.matdes.2017.02.016.

[40] B. Abendroth, T. Moebus, S. Rentrop, R. Strohmeyer, M. Vinnichenko, T. Weling, H. Stöcker, D.C. Meyer, Atomic layer deposition of TiO 2 from tetrakis(dimethylamino)titanium and H 2 O, Thin Solid Films. 545 (2013) 176–182. https://doi.org/10.1016/j.tsf.2013.07.076.

[41] Q. Xie, Y.-L. Jiang, C. Detavernier, D. Deduytsche, R.L. Van Meirhaeghe, G.-P. Ru, B.-Z. Li, X.-P. Qu, Atomic layer deposition of TiO2 from tetrakis-dimethyl-amido titanium or Ti isopropoxide precursors and H2O, J. Appl. Phys. 102 (2007) 083521. https://doi.org/10.1063/1.2798384.

[42] M.E. Dufond, M.W. Diouf, C. Badie, C. Laffon, P. Parent, D. Ferry, D. Grosso, J.C.S. Kools, S.D. Elliott, L. Santinacci, Quantifying the Extent of Ligand Incorporation and the Effect on Properties of TiO2 Thin Films Grown by Atomic Layer Deposition Using an Alkoxide or an Alkylamide, Chem. Mater. 32 (2020) 1393–1407. https://doi.org/10.1021/acs.chemmater.9b03621.

[43] C. Byrne, R. Fagan, S. Hinder, D.E. McCormack, S.C. Pillai, New approach of modifying the anatase to rutile transition temperature in TiO 2 photocatalysts, RSC Adv. 6 (2016) 95232–95238. https://doi.org/10.1039/C6RA19759K.

[44] L. Palmolahti, H. Ali-Löytty, M. Hannula, J. Saari, W. Wang, A. Tukiainen, K. Lahtonen, M. Valden, Pinhole-Resistant Nanocrystalline Rutile TiO 2 Photoelectrode

Coatings, SSRN Electron. J. (2022). https://doi.org/10.2139/ssrn.4059728.

[45] L. Tsetseris, Stability and dynamics of carbon and nitrogen dopants in anatase TiO2 : A density functional theory study, Phys. Rev. B. 81 (2010) 165205. https://doi.org/10.1103/PhysRevB.81.165205.

[46] X. Chen, L. Liu, P.Y. Yu, S.S. Mao, Increasing Solar Absorption for Photocatalysis with Black Hydrogenated Titanium Dioxide Nanocrystals, Science (80-.). 331 (2011) 746–750. https://doi.org/10.1126/science.1200448.

[47] D.A. Shirley, High-resolution x-ray photoemission spectrum of the valence bands of gold, Phys. Rev. B. 5 (1972) 4709–4714. https://doi.org/10.1103/PhysRevB.5.4709.

[48] R. Dziembaj, Z. Piwowarska, X-ray photoelectron spectroscopy (XPS) as a useful tool to characterize polyaniline doped by 12-tungstosilicic, 12-tungstophosphoric and 12-molybdophosphoric acids, Synth. Met. 63 (1994) 225–232. https://doi.org/10.1016/0379-6779(94)90233-X.

[49] A. Zakhtser, A. Naitabdi, R. Benbalagh, F. Rochet, C. Salzemann, C. Petit, S. Giorgio, Chemical Evolution of Pt–Zn Nanoalloys Dressed in Oleylamine, ACS Nano. 15 (2021) 4018–4033. https://doi.org/10.1021/acsnano.0c03366.

[50] E. Farfan-Arribas, R.J. Madix, Characterization of the Acid−Base Properties of the TiO 2 (110) Surface by Adsorption of Amines, J. Phys. Chem. B. 107 (2003) 3225–3233. https://doi.org/10.1021/jp022344c.

[51] L. Mohrhusen, L. Gerhards, D. Hirsch, T. Klüner, K. Al-Shamery, Multidentate Interaction of Methylamine with Rutile TiO 2 (110), J. Phys. Chem. C. 125 (2021) 11975–11986. https://doi.org/10.1021/acs.jpcc.1c02166.

[52] A. Hemeryck, A. Motta, C. Lacaze-Dufaure, D. Costa, P. Marcus, DFT-D study of adsorption of diaminoethane and propylamine molecules on anatase (101) TiO 2 surface, Appl. Surf. Sci. 426 (2017) 107–115. https://doi.org/10.1016/j.apsusc.2017.07.161.

[53] T.K. Sham, M.S. Lazarus, X-ray photoelectron spectroscopy (XPS) studies of clean and hydrated TiO2 (rutile) surfaces, Chem. Phys. Lett. 68 (1979) 426–432. https://doi.org/10.1016/0009-2614(79)87231-0.

[54] C.E. Patrick, F. Giustino, Structure of a Water Monolayer on the Anatase TiO2 (101) Surface, Phys. Rev. Appl. 2 (2014) 014001. https://doi.org/10.1103/PhysRevApplied.2.014001.

[55] G. Liu, L.-C. Yin, J. Wang, P. Niu, C. Zhen, Y. Xie, H.-M. Cheng, A red anatase TiO2 photocatalyst for solar energy conversion, Energy Environ. Sci. 5 (2012) 9603. https://doi.org/10.1039/c2ee22930g.

[56] M.E. Arroyo-de Dompablo, A. Morales-García, M. Taravillo, DFT+ U calculations of crystal lattice, electronic structure, and phase stability under pressure of TiO 2 polymorphs, J. Chem. Phys. 135 (2011) 054503. https://doi.org/10.1063/1.3617244.

[57] Z. Wang, U. Helmersson, P.-O. Käll, Optical properties of anatase TiO2 thin films prepared by aqueous sol–gel process at low temperature, Thin Solid Films. 405 (2002) 50–54. https://doi.org/10.1016/S0040-6090(01)01767-9.

[58] T. Luttrell, S. Halpegamage, J. Tao, A. Kramer, E. Sutter, M. Batzill, Why is anatase a better photocatalyst than rutile? - Model studies on epitaxial TiO2 films, Sci. Rep. 4 (2015) 4043. https://doi.org/10.1038/srep04043.

[59] E. V. Lavrov, I. Chaplygin, F. Herklotz, V. V. Melnikov, Y. Kutin, Hydrogen in single-crystalline anatase TiO 2, J. Appl. Phys. 131 (2022) 030902. https://doi.org/10.1063/5.0076694.

[60] Y. Yang, L.-C. Yin, Y. Gong, P. Niu, J.-Q. Wang, L. Gu, X. Chen, G. Liu, L. Wang, H.-M. Cheng, An Unusual Strong Visible-Light Absorption Band in Red Anatase TiO 2 Photocatalyst Induced by Atomic Hydrogen-Occupied Oxygen Vacancies, Adv. Mater. 30 (2018) 1704479. https://doi.org/10.1002/adma.201704479.

[61] X. Chen, L. Liu, Z. Liu, M.A. Marcus, W.-C. Wang, N.A. Oyler, M.E. Grass, B. Mao, P.-A. Glans, P.Y. Yu, J. Guo, S.S. Mao, Properties of Disorder-Engineered Black Titanium Dioxide Nanoparticles through Hydrogenation, Sci. Rep. 3 (2013) 1510. https://doi.org/10.1038/srep01510.